Materials Characterization 119 (2016) 84–91

Contents lists available at ScienceDirect

Materials Characterization

journal homepage: www.elsevier.com/locate/matchar

Microstructure, texture, and mechanical properties of friction stir welded commercial brass alloy

A. Heidarzadeh [a,b], T. Saeid [b,*], V. Klemm [c]

[a] Department of Materials Engineering, Azarbaijan Shahid Madani University, Tabriz, Iran
[b] Faculty of Materials Engineering, Sahand University of Technology, Tabriz, Iran
[c] Institute of Materials Science, Technische Universität Bergakademie Freiberg, Germany

ARTICLE INFO

Article history:
Received 17 January 2016
Received in revised form 9 July 2016
Accepted 11 July 2016
Available online 12 July 2016

Keywords:
Friction stir welding
Microstructure
Texture
Mechanical properties

ABSTRACT

Microstructural evolution during friction stir welding of single-phase brass and corresponding mechanical properties were investigated. For this purpose, 2 mm thick brass plate was friction stir welded at a rotational speed of 450 rpm and traverse speed of 100 mm/min. The microstructure of the joint was studied using optical microscopy, scanning electron microscopy equipped with electron back scattered diffraction system, and scanning transmission electron microscopy. The mechanical properties were measured using hardness and tensile tests. The formation of subgrains and their transformation into new grains in conjunction with existence of A_1^*, A_2^* and C texture components revealed that the continuous dynamic recrystallization plays a dominant role in the microstructural evolution. However, grain boundary bulging, along with the formation of twin boundaries, and presence of the G texture component showed that the discontinues dynamic recrystallization may participate in the new grain formation. Furthermore, the different strengthening mechanisms, which caused the higher strength of the joint, were discussed.

1. Introduction

Friction stir welding (FSW) was developed at The Welding Institute of UK in 1991 [1]. It is a solid-state welding method without large distortion, solidification cracking, porosity, oxidation, and other defects that arise from conventional fusion welding [2]. In addition, it can improve the mechanical properties of the joints compared to fusion welding processes. Therefore, FSW has been proved a promising joining method for various metals and alloys [1,3].

Brasses, the copper and zinc alloys, have vast industrial applications, and so there is a large demand for welding of these types of alloys. Unfortunately, the conventional fusion welding of brasses has some difficulties in addition to the common problems mentioned before. The low boiling temperature of the zinc causes to its evaporation during fusion welding processes, which results in color change and formation of a porous and weak layer of copper or copper oxide. Additionally, it is notable that the zinc vapor is toxic and can be harmful to the health of welding operator. Therefore, the investigators have been encouraged to use FSW for joining of the brass alloys.

Despite a lot of investigations in the field of copper FSW, the studies in the case of brass alloys are somewhat limited [4–12]. Xie et al. [9,12] have studied the effect of FSW on the microstructure and mechanical properties of 5 mm thick 62/38 brass plates. They reported that partial recrystallization occurred during FSW, which caused the formation of different types of grains, including recrystallized, deformed recrystallized and deformed grains in the stir zone (SZ) of the joints. They also found that the high heat input conditions, i.e. higher rotational speeds and lower traverse speeds of the tool, resulted in a more homogenized structure in the SZ, but could not completely remove the partially recrystallized zone. Xu et al. [10] have used rapid cooling during FSW of 2 mm thick 70/30 brass plates to improve the mechanical properties of the welded joints. They confirmed that with rapid cooling, the grain size of 1.2 μm was achieved, and the post annealing effect, including both recovery and static recrystallization could be prohibited. Emamikhah et al. [13] have investigated the effect of tool pin profile in FSW of 3 mm thick 60/40 brass plates. Their results showed that appropriate tools can produce sufficient heat underneath the shoulder with regard to further materials stirring. Additionally, they demonstrated that a hexahedron tool caused the accumulated defects, and hence the mechanical properties weakened due to a lower heat generated.

FSW can be assumed as a kind of hot deformation processes in some aspects due to existence of heat and deformation. Thus, the restoration

* Corresponding author.
E-mail addresses: ak.hz62@gmail.com, a_heidarzadeh@sut.ac.ir (A. Heidarzadeh), saeid@sut.ac.ir (T. Saeid).

http://dx.doi.org/10.1016/j.matchar.2016.07.009
1044-5803/

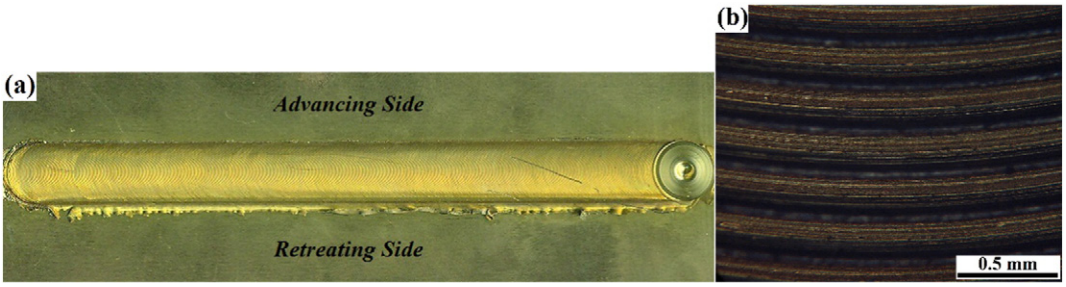

Fig. 1. (a) Surface of the joint, and (b) higher magnification of (a).

mechanisms of hot deformation processes can occur during FSW of metals which rule the final microstructure and mechanical properties [14–16]. Some researchers [17–23] have studied the microstructural evolution during FSW of different metals and alloys. They have concluded that the dynamic recovery (DRV), discontinuous dynamic recrystallization (DDRX), continuous dynamic recrystallization (CDRX), geometrical dynamic recrystallization (GDRX) and static recrystallization (SRX) take place during FSW of various materials similar to other hot deformation processes. However, because of sharp gradients in strain, strain rate, and temperature during FSW, the restoration mechanisms will be different from conventional hot deformation processes of the same alloys, which comprise almost uniform strains and temperatures [24,25].

Although some researchers [4–12] have studied FSW of brass plates, an investigation into the deep microstructural aspects and their relation to the final mechanical properties of the joint is lacking. Therefore, the objectives of this study are to determine the type of restoration mechanisms during FSW of single-phase brass plates, and to realize the strengthening mechanisms of the welded joint.

2. Materials and methods

The single-phase brass (70% Cu and 30% Zn) plate with an initial cold worked condition was used as a base metal (BM) with dimensions of 150 mm × 100 mm × 2 mm. This composition of brasses belongs to the cartridge brass, which has a wide application among the other types of brasses. In addition, because of its single-phase microstructure, it was suitable for the aim of the present study. The BM was annealed at 500 °C for 1 h, before FSW. A H13 steel tool with a shoulder (12 mm diameter) and a simple cylindrical pin (3 mm diameter and 1.7 mm length) was used at a rotational speed of 450 rpm and traverse speed of 100 mm/min. The selection of the H13 steel tool for FSW of the brass plate was according to the literature and our previous laboratory experiences [4–12].

The macrostructure of the joint cross section was analyzed using optical microscopy (OM). The metallographic samples were cut from the section perpendicular to the welding direction, then polished and etched with a solution of 20 ml nitric acid and 10 ml acetic acid. A JEOL JSM 6500F field emission scanning electron microscopy (FESEM) equipped with electron backscatter diffraction (EBSD) system (HKL) was used for microstructural and textural characterizations. In order to produce a suitable surface finish of EBSD sample, the electropolishing was conducted in a solution including 250 ml H_3PO_4, 250 ml ethanol, 50 ml propanol, 500 ml distilled water, and 3 g urea under an applied potential of 10 V for 30 s. In addition, the microstructure of the joint was characterized using transmission electron microscopy (TEM, JEM 2200FS). For this aim, jet thinning was used to produce the thin films for TEM investigations.

In order to study the mechanical properties, the Vickers microhardness test was performed using 50 g load for 10 s. In addition, the tensile test specimens were machined perpendicular to the welding direction with a gauge size of 12 mm (length) × 3 mm (width) × 2 mm (thickness), and tensile tests were conducted at a crosshead speed of 1 mm/min.

3. Results and discussion

3.1. Microstructure

The surface of the joint is illustrated in Fig. 1a, which shows that the joint has excellent surface appearance, with regular grooves. Also, the higher magnification of the weld surface (Fig. 1b) indicated that the tool revolution per mm was approximately equal to 4.5 which confirms the used FSW parameters in this study i.e. 450 rpm and 100 mm/min.

The macrostructure of the joint is shown in Fig. 2, which indicates that the joint was defect free. Furthermore, it can be seen that the macrostructure consists of three distinct regions, including BM, thermomechanically affected zone (TMAZ) and SZ. The optical microstructure of these three regions at higher magnification are illustrated in Fig. 3. The absence of heat-affected zone (HAZ) in the macrostructure of the joint can be due to high thermal conductivity of the brass and low heat input condition of the present study. Moreover, the difference between the size and morphology of the SZ and TMAZ grains makes sharp and clear the interface of these microstructural zones.

The grain boundary maps of the different zones of the joint macrostructure are illustrated in Figs. 4-6. As well, the corresponding distribution of misorientation angle and different types of grain boundaries are shown in Figs. 7 and 8. From Figs. 4–8, the BM had a coarse grain

Fig. 2. The cross sectional macrostructure of the joint.

Fig. 3. The combined optical microstructure showing different zones of BM, TMAZ and SZ in advancing side of the joint.

structure with 32% of high-angle grain boundaries (HAGBs), 3% of low-angle grain boundaries (LAGBs) and 65% of twin boundaries (TBs). According to the Figs. 7 and 8, the 67% of the total HAGBs were characterized as TBs. These TBs are Σ3 coincidence site lattice (CSL) boundaries which are rotated 60° about ⟨111⟩ axis in face centered cubic (FCC) materials [22].

The high amount of Σ3 boundaries may refer to the formation of TBs during recrystallization and grain growth of the BM. The microstructure of TMAZ revealed a deformed structure with elongated grains, high amount of LAGBs (58%), low value of Σ3 boundaries (7%), and 35% of HAGBs. Furthermore, SZ contained fine equiaxed grains, 27% of LAGBs, 18% of Σ3 boundaries, and 55% of HAGBs. The considerable variation of grain size from BM to SZ is the evidence that the SZ grains have recrystallized during FSW. Mironov et al. [26] and Jeon et al. [20] have studied the recrystallization mechanisms during FSW of pure copper and single-crystal austenitic stainless steel with medium and low stacking fault energies (SFEs), respectively. They have reported that both the CDRX and DDRX mechanisms cause to formation of fine equiaxed grains. Moreover, Saeid et al. [22] have found that the austenite phase (with low SFE) in a duplex stainless steel undergoes CDRX and SRX during FSW. The common outcome of these studies is that CDRX can be one of the main mechanisms during FSW of materials with low to medium SFEs.

CDRX consists of the following stages: (i) DRV of the dislocations and formation of the subgrains, (ii) absorption of the dislocations to the subgrains and gradual increasing the misorientation of the LAGBs up to that of the HAGBs. Thus, during CDRX there are not any distinct nucleation and growth stages, and the deformation textures are usually remained in the structure [27,28]. From Fig. 5, the subgrains form near the old grain boundaries and inside the grains (indicated by red arrow). It can be concluded that such subgrains form with approximately the same size of the SZ grains (Figs. 5 and 6). Also, the fraction of the LAGBs and HAGBs decreases and increases from TMAZ to SZ (Figs. 7 and 8), respectively. Furthermore, there are some LAGBs, which are partly transformed to HAGBs in some regions of the TMAZ (indicated by black arrows in Fig. 5). These evidences demonstrate that the subgrain boundaries transform into the grain boundaries during FSW. Therefore, these results suggest that CDRX may rule the formation of SZ grain structure. In addition, it is observed that some grain boundaries are serrated (Fig. 5) which can be the sign of GDRX. Prangnell et al. [21], Etter et al. [18], and McNelley et al. [24] have demonstrated that GDRX occurs during FSW of AA2195, AA 5251, and AA2099 aluminum alloy plates, respectively. In GDRX, the DRV causes the formation of subgrains and serrations in prior grain boundaries that have wavelengths similar to the subgrain sizes. By increasing the strain, the old grains are pancaked, the fraction of HAGBs increases, and the size of the serrations turn approximately equal into the thickness of the pancaked grains. Then, the opposite serrated boundaries meet each other and causes the conversion of the old grains into fine equiaxed grains with sizes similar to the subgrain sizes [27,28]. Therefore, it is expected that the adjacent grains formed during GDRX would have a small misorientation along the deformation direction. Fig. 9 shows the misorientation changes of the recrystallized grains inside the TMAZ along the line AB (Fig. 5). According to Fig. 9, the neighboring grains show high misorientations along the line AB, which disproves the occurrence of GDRX.

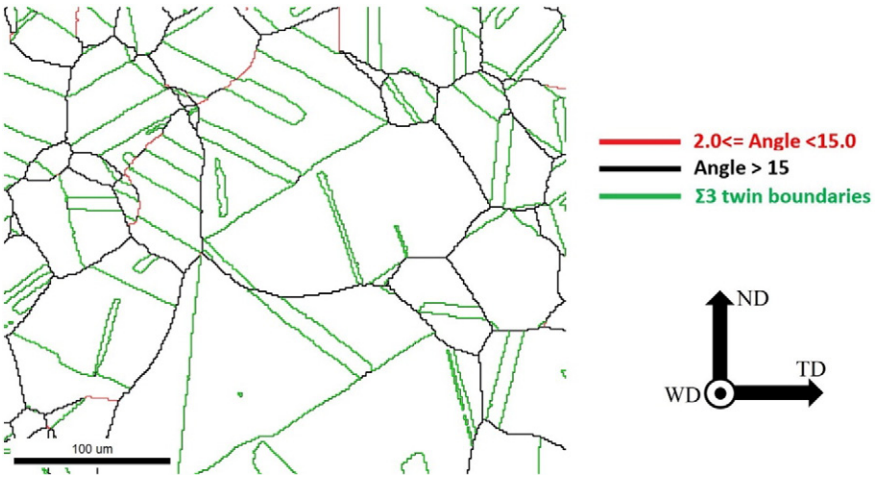

Fig. 4. Grain boundary map of the BM. The black, red, and green lines in EBSD maps correspond to the HAGBs ($\theta \geq 15°$), LAGBs ($2° < \theta < 15°$), and Σ3 twin boundaries, respectively. These features are used in all EBSD maps in this paper.

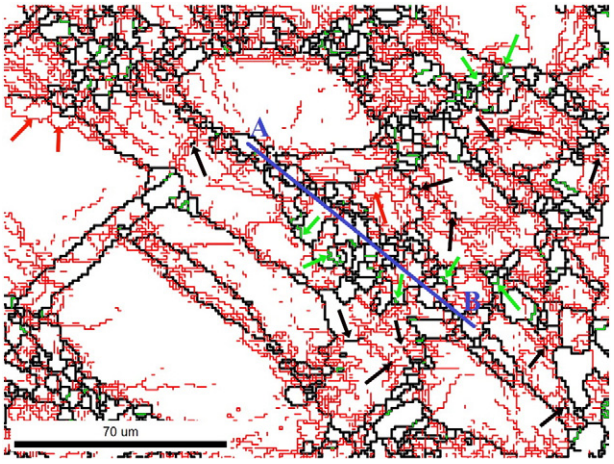

Fig. 5. Grain boundary map of the TMAZ.

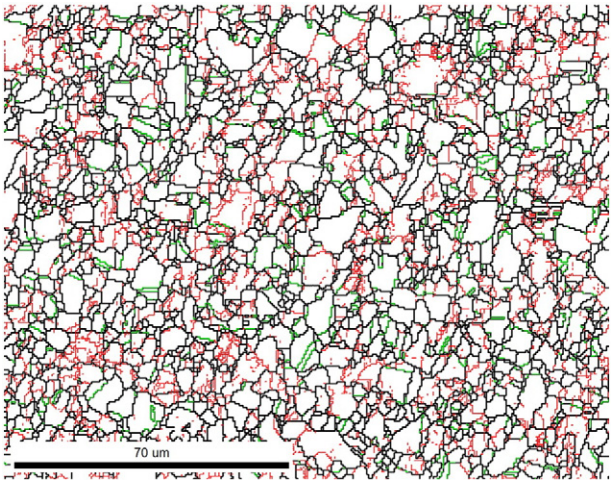

Fig. 6. Grain boundary map of the SZ.

In addition to CDRX and GDRX, the DDRX can happen during FSW [16,20,23,25]. DDRX [25–27] typically occurs in hot defamation processes of the materials with low to medium SFE, and it has two distinct stages of the nucleation and growth [27–29]. The stages of the DDRX can be summarized as follows: (i) boundary serration together with the development of dislocation sub boundaries, (ii) the grain boundary shearing or sliding (GBS) and the development of local strain gradients (plastic accommodation), and (iii) the bulging out of the serrated parts along with the development of sub boundaries or twin boundaries [24,29].

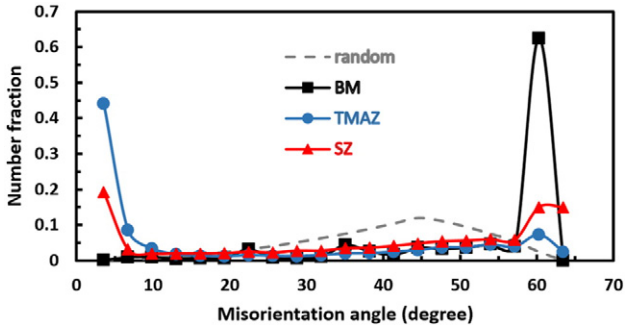

Fig. 7. Misorientation angle distributions driven from the EBSD maps shown in Figs. 4–6. The random distribution is illustrated by a dotted grey line, which is drawn by EBSD software according to the Mackenzie random distribution.

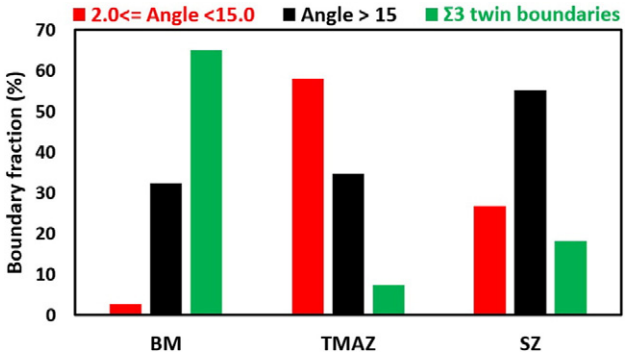

Fig. 8. HAGB, LAGB and Σ3 boundary fraction within the different microstructural regions.

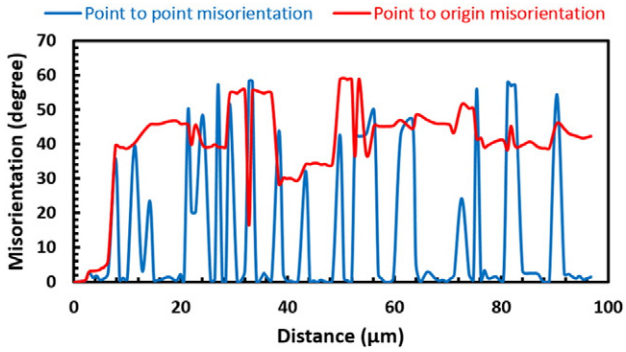

Fig. 9. Misorientation variance along the AB line shown in Fig. 5.

From Figs. 7 and 8, the fraction of the Σ3 boundaries decreases from BM to TMAZ, which is associated with the strain induced crystallographic rotations of the twins from their original orientations [17].

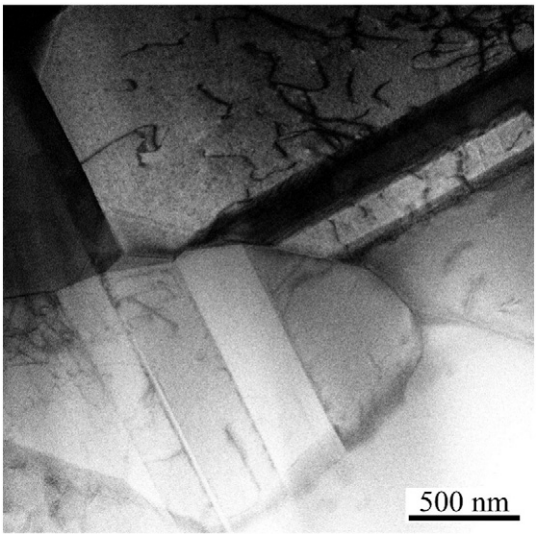

Fig. 10. STEM image of the SZ showing formation of twin lamellas in this area.

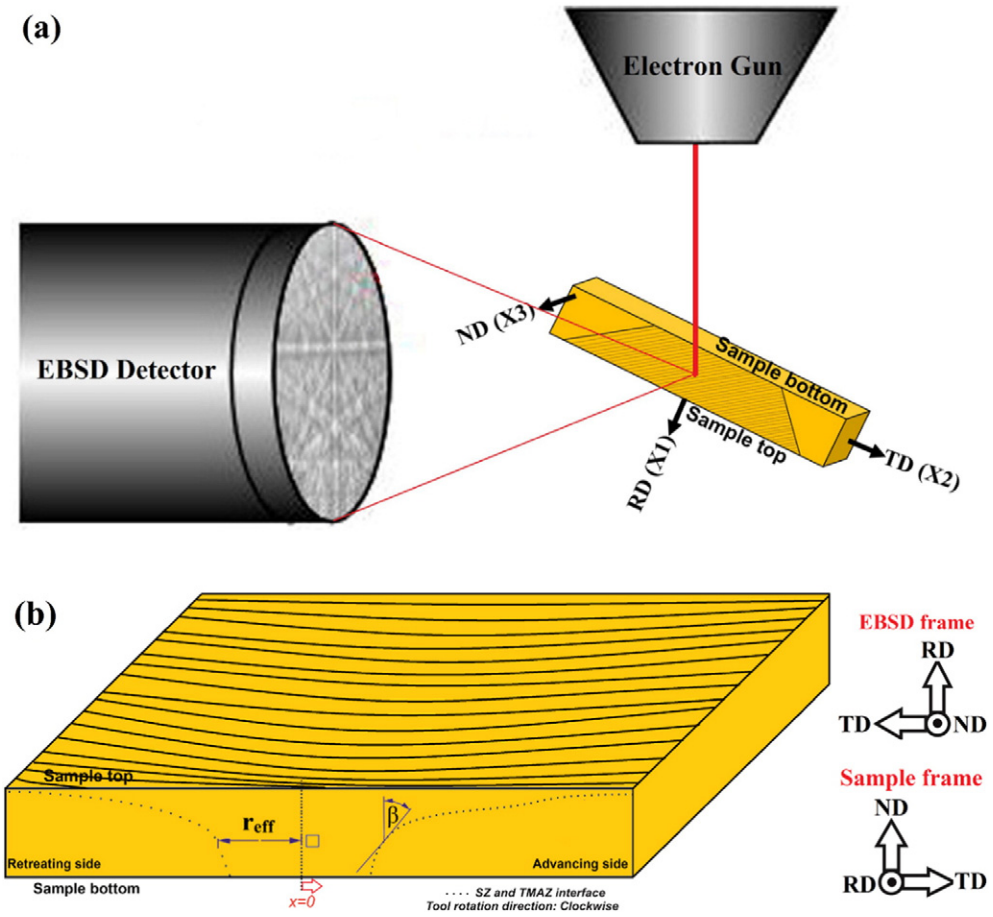

Fig. 11. (a) The schematic illustration of sample orientation in the EBSD chamber during analyzing, and (b) Schematic of the sample surface.

In addition, the Σ3 boundaries increase from TMAZ to SZ, which can be due to the formation of TBs during DDRX. From Fig. 5, some evidence of boundary bulging and twin formations can be distinguished (indicated by green arrows) which suggests the occurrence of DDRX. Therefore, the SZ grains appear to be created as a result of both CDRX and DDRX. In order to determine the contribution of these two mechanisms, textural studies were conducted which will be discussed later. Furthermore, after DRX, the growth of SZ grains can occur with the formation of TBs in the form of twin lamellas as shown in Figs. 10. The formation mechanism of such TBs has been modeled before based on energy criterion [27].

3.2. Texture

The texture components developed in SZ of the joints are usually recognized by comparison with ideal shear texture components which have been reported in the literature in a standard frame of reference with the shear direction (SD) pointing right and the shear plane normal (SPN) pointing up. For this purpose, two types of rotations are needed before comparison: (i) rotations in order to coincide the EBSD software reference frame with the local shear frame of reference, and (ii) rotations according to the difference between the obtained texture orientation and the local shear surface orientation of the shear surface. According to rotation types (i) and the schematics shown in Fig. 11, to coincident the EBSD and sample reference frames 180° about normal direction (ND) and 90° about traverse direction (TD) were applied to the as-acquired pole figures (PFs). Similarly, so as to rotations type (ii), the α and β are needed to be calculated. The α comes from the rotation of shear direction about the rotating tool and β comes from the inclination of shear plane as a function of depth in the weld [30]. The α can be calculated according the following equation [30]:

$$\alpha = sin^{-1}\left(\frac{x}{r_{eff}}\right) \quad (1)$$

Where x is the distance between the weld center and the region that EBSD is taken, and r_{eff} stands for the effective radius of the shear surface at a specific depth of the weld. In this study the x/r_{eff} was equal to 0.15, and hence the α was approximately 9°. In addition, the β was measured approximately equal to 40° as illustrated in Fig. 11. Finally, the PFs should be reported using SD, SPN and RA (rotation axis). At weld center, the SD, SPN and RA are parallel to TD, RD (rolling direction) and ND, respectively. According to the final step, the replacement of the TD with SD and RD with SPN results in the final PF in standard frame.

The as-acquired and rotation sequences of the PFs of the SZ, and the corresponding orientation distribution functions (ODF) of the final rotated PF are illustrated in Figs. 12 and 13, respectively. Moreover, the ideal recrystallization and simple shear texture components of the face centered cubic metals are summarized in Table 1. Fig. 13 and Table 1 reveals that the A_1^*, A_2^* and C are the predominant texture components in the SZ of the joint. Furthermore, the Goss (G) component is also existent to some extent, and the Cube component is nonexistent. The A_1^*, A_2^* and C are ideal orientations in simple shear deformation of face-centered cubic (FCC) materials which confirm the occurrence of CDRX, because CDRX happen along with retaining the deformation textures [24]. Conversely, DDRX leads to replacement of deformation

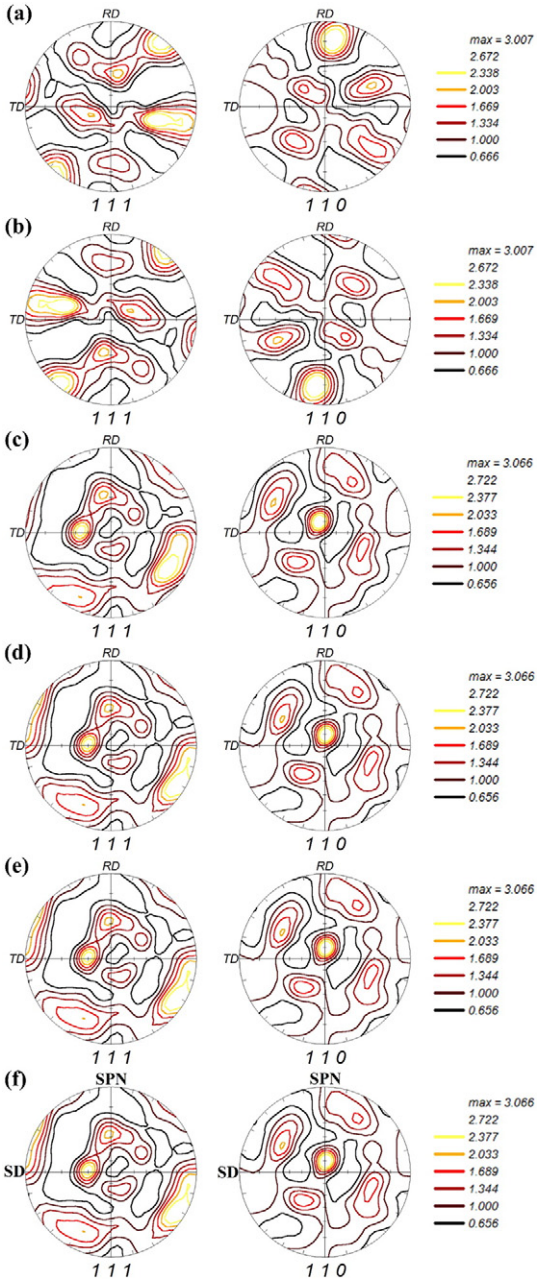

Fig. 12. (a) As-acquired (111) and (110) PFs of the SZ, (b) after 180° rotation about ND, (c) after 90° rotation about TD, (d) after rotation by α (9° about RD), (e) after rotation by β (40° about TD), and (f) after alignments of SPN with RD and SD with TD.

textures with typical recrystallization textures [24]. Thus, the presence of the G component in SZ, which is one of the common recrystallization texture components, can be associated with occurrence of DDRX. According to the texture results, it can be recognized that the shear texture components are the main components in the SZ of the joint. Thus, it can be concluded that CDRX is the dominant mechanism during FSW of single-phase brass. Also, the nonexistence of Cube component, which is the most common SRX texture component in FCC metals [22,27], reveals that the SRX could not be happened.

3.3. Mechanical properties

The hardness profile and the engineering strain–stress curve (Figs. 14 and 15) disclose that the hardness and strength of the joint are higher than those of the BM. The strengthening mechanisms in polycrystalline metals and alloys, which result in higher critical resolved shear stress (CRSS) of the slip planes, can be classified as the precipitation strengthening ($\Delta\tau_{ppt}$), the solution strengthening ($\Delta\tau_{ss}$), the dislocation strengthening ($\Delta\tau_D$), the grain boundary strengthening ($\Delta\sigma_{gb}$), and the texture strengthening. Consequently, the yield strength (σ_y) can be stated as follows [31]:

$$\sigma_y = \Delta\sigma_{gb} + M\tau_{tot} = \Delta\sigma_{gb} + M\left[\Delta\tau_0 + \Delta\tau_{ss} + \left(\Delta\tau_D^2 + \Delta\tau_{ppt}^2\right)^{1/2}\right] \quad (1)$$

where M stands for crystallographic orientation factor (usually the Taylor factor), τ_{tot} represents the CRSS and $\Delta\tau_0$ belongs to the intrinsic strength of pure metal. According to Eq. (1) and the point that the BM was a single-phase alloy without precipitates, the strengthening mechanisms causing dissimilar strengths in BM and joint are $\Delta\sigma_{gb}$, $\Delta\tau_D$ and the texture influence. The strength due to the grain boundaries in a recrystallized metal can be formulated as follows [32]:

$$\Delta\sigma_{gb} = \alpha_2 Gb\left[(1-f_{Re})\left(1/\delta\right) + f_{Re}\left(1/D\right)\right] \quad (2)$$

where α_2 stands for a constant, G refers to the shear modulus, b belongs to the Burgers vector, f_{Re} represents the recrystallized volume fraction, σ states the subgrain size of the unrecrystallized part, and the D denotes the grain size of the recrystallized part.

According to the Eq. (2) and the EBSD maps of the BM, TMAZ and SZ (Figs. 4–6), $\Delta\sigma_{gb}$ of the SZ and TMAZ will have larger amounts than that of the BM. Furthermore, the rise in CRSS owing to dislocations can be formulated as following equation [33]:

$$\Delta\sigma_D = \alpha_1 Gb\sqrt{\rho} \quad (3)$$

where α_2 refers to a constant and ρ stands for the dislocation density. According to the STEM images of the BM, SZ and TMAZ (Figs. 10, 16a–b), it is clear that the dislocation density in the TMAZ and SZ are higher

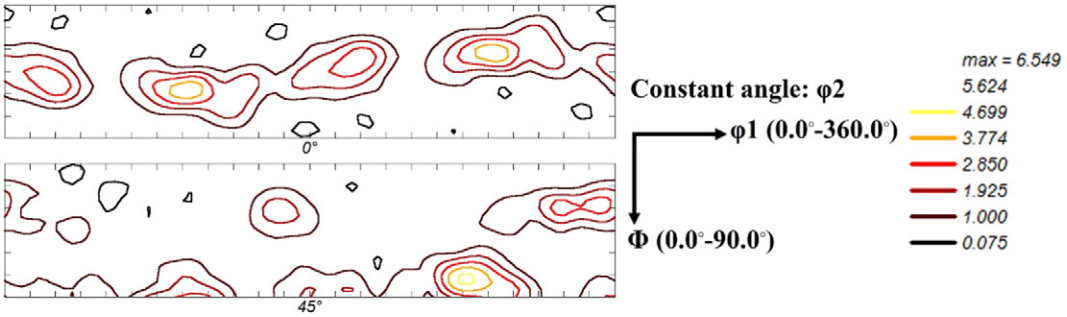

Fig. 13. The ODF sections of final PFs shown in Fig. 12f at φ2 = 0° and φ2 = 45°.

Table 1
Main ideal orientations in simple shear deformation and recrystallization in FCC metals [27].

Notation	Miller indices	Euler angles (°)		
		φ_1	Φ	φ_2
(Simple shear deformation)				
A_1^*	$(111)[\bar{1}\bar{1}2]$	35.26/215.26	45	0/90
		125.26	90	45
A_2^*	$(111)[11\bar{2}]$	144.74	45	0/90
		54.74/234.74	90	45
A	$(1\bar{1}1)[110]$	0	35.26	45
$\bar{A}$	$(\bar{1}1\bar{1})[\bar{1}10]$	180	35.26	45
B	$(1\bar{1}2)[110]$	0/120/240	54.74	45
$\bar{B}$	$(\bar{1}1\bar{2})[\bar{1}10]$	60/180	54.74	45
C	{001}⟨110⟩	90/270	45	0/90
		0/180	90	45
(Recrystallization)				
Cube	{001}⟨100⟩	0	0	0
–	{236}⟨385⟩	79	31	33
Goss (G)	{011}⟨100⟩	0	45	0
S	{123}⟨634⟩	59	37	63
P	{011}⟨122⟩	70	45	0
Q	{013}⟨231⟩	58	18	0
R	{124}⟨211⟩	57	29	63

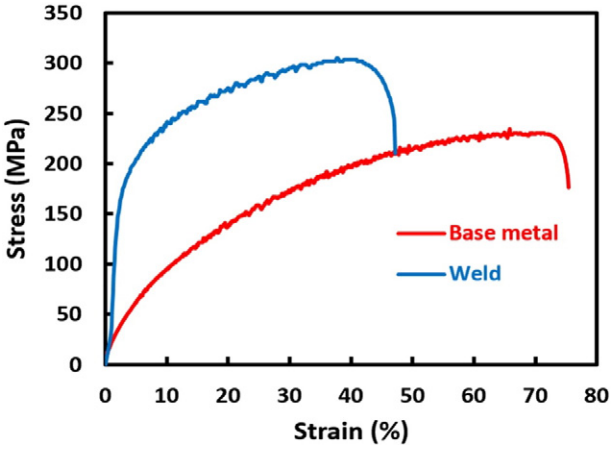

Fig. 15. Engineering stress-strain curves of the BM and joint.

during FSW, the DDRX occurred to some extent, and the GDRX and SRX were not happened. The lamellas TBs were formed in the SZ due to growth of recrystallized grains. Three strengthening mechanisms, than that of the BM, which will cause to larger values of $\Delta\tau_D$. Additionally, the influence of crystallographic texture on the strength has been presented in term of the factor M in Eq. (1). For exploring the effect of factor M, the Taylor factor in the different regions of the BM, TMAZ and SZ have been calculated from EBSD data for both compression along RD (microhardness tests) and tension along TD (tensile tests). The Taylor factors were estimated 2.92, 2.94, and 3.11 in the case of microhardness tests, and 3.04, 3.14, and 3.08 in the case of tensile tests for BM, TMAZ and SZ, respectively. Therefore, the Taylor factors of the SZ and TMAZ are higher than that of the BM, which leads to higher M and consequently higher strength.

4. Conclusion

In summary, the evolution of microstructure during FSW of a single-phase brass alloy and corresponding strengthening mechanism were investigated using EBSD and TEM techniques. The microstructure, fraction of HAGBs, LAGBs and Σ3 TBs, and texture analysis of the BM, TMAZ and SZ revealed that the CDRX was the dominant restoration mechanism

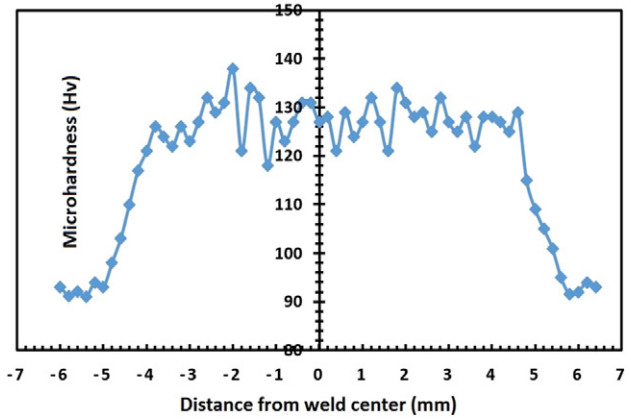

Fig. 14. Hardness profile of the joint along centerline of its cross section.

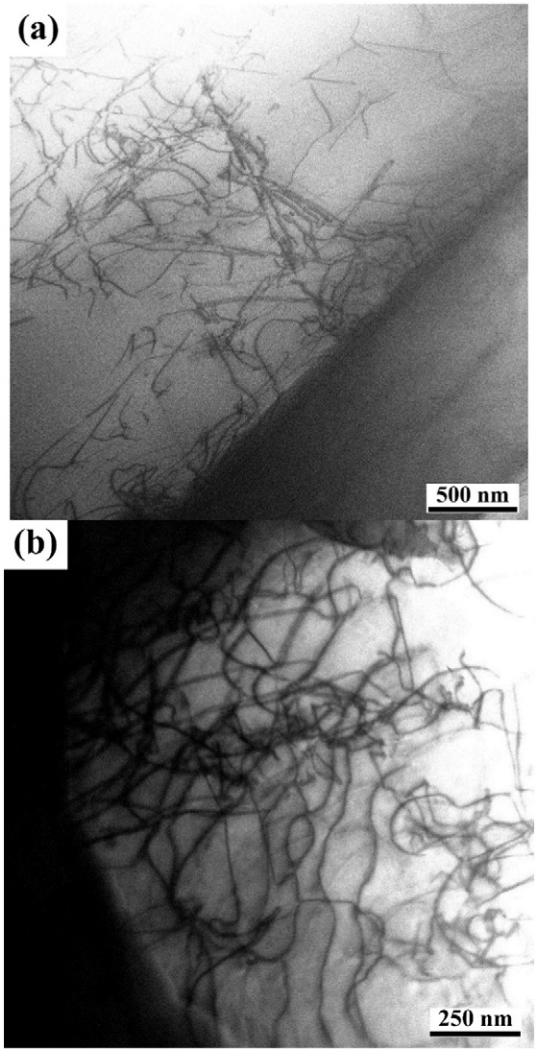

Fig. 16. (a) STEM image of the BM showing an annealing twin and low density of dislocations, and (b) STEM image of the TMAZ displaying high density of dislocations.

including grain boundary, dislocation and strengthening due to crystallographic texture were identified as the main reasons of the higher hardness and strength of the joint compared to BM.

References

[1] S. Kundu, D. Roy, R. Bhola, D. Bhattacharjee, B. Mishra, S. Chatterjee, Microstructure and tensile strength of friction stir welded joints between interstitial free steel and commercially pure aluminium, Mater. Des. 50 (2013) 370–375.
[2] A. Heidarzadeh, T. Saeid, Prediction of mechanical properties in friction stir welds of pure copper, Mater. Des. 52 (2013) 1077–1087.
[3] Y. Mao, L. Ke, F. Liu, Q. Liu, C. Huang, L. Xing, Effect of tool pin eccentricity on microstructure and mechanical properties in friction stir welded 7075 aluminum alloy thick plate, Mater. Des. 62 (2014) 334–343.
[4] A. Heidarzadeh, T. Saeid, A comparative study of microstructure and mechanical properties between friction stir welded single and double phase brass alloys, Mater. Sci. Eng. A 649 (2016) 349–358.
[5] A. Heidarzadeh, T. Saeid, Correlation between process parameters, grain size and hardness of friction-stir-welded Cu–Zn alloys, Rare Met. (2016) (in press).
[6] G. Çam, H.T. Serindağ, A. Çakan, S. Mistikoglu, H. Yavuz, The effect of weld parameters on friction stir welding of brass plates, Mater. Werkst. 39 (2008) 394–399.
[7] C. Meran, The joint properties of brass plates by friction stir welding, Mater. Des. 27 (2006) 719–726.
[8] H. Khodaverdizadeh, A. Mahmoudi, A. Heidarzadeh, E. Nazari, Effect of friction stir welding (FSW) parameters on strain hardening behavior of pure copper joints, Mater. Des. 35 (2012) 330–334.
[9] G.M. Xie, Z.Y. Ma, L. Geng, Effects of friction stir welding parameters on microstructures and mechanical properties of brass joints, Mater. Trans. 49 (2008) 1698–1701.
[10] N. Xu, R. Ueji, H. Fujii, Enhanced mechanical properties of 70/30 brass joint by rapid cooling friction stir welding, Mater. Sci. Eng. A 610 (2014) 132–138.
[11] S. Mironov, K. Inagaki, Y.S. Sato, H. Kokawa, Development of grain structure during friction-stir welding of Cu–30Zn brass, Philos. Mag. 94 (2014) 3137–3148.
[12] G.M. Xie, Z.Y. Ma, L. Geng, Partial recrystallization in the nugget zone of friction stir welded dual-phase Cu–Zn alloy, Philos. Mag. 89 (2009) 1505–1516.
[13] A. Emamikhah, A. Abbasi, A. Atefat, M.K.B. Givi, Effect of tool pin profile on friction stir butt welding of high-zinc brass (CuZn40), Int. J. Adv. Manuf. Technol. 71 (2014) 81–90.
[14] Y.S. Sato, Y. Nagahama, S. Mironov, H. Kokawa, S.H.C. Park, S. Hirano, Microstructural studies of friction stir welded Zircaloy-4, Scr. Mater. 67 (2012) 241–244.
[15] Y.S. Sato, H. Yamanoi, H. Kokawa, T. Furuhara, Microstructural evolution of ultrahigh carbon steel during friction stir welding, Scr. Mater. 57 (2007) 557–560.
[16] S. Mironov, Y.S. Sato, H. Kokawa, Development of grain structure during friction stir welding of pure titanium, Acta Mater. 57 (2009) 4519–4528.
[17] J. Jeon, S. Mironov, Y.S. Sato, H. Kokawa, S.H.C. Park, S. Hirano, Friction stir spot welding of single-crystal austenitic stainless steel, Acta Mater. 59 (2011) 7439–7449.
[18] A.L. Etter, T. Baudin, N. Fredj, R. Penelle, Recrystallization mechanisms in 5251 H14 and 5251 O aluminum friction stir welds, Mater. Sci. Eng. A 445–446 (2007) 94–99.
[19] R.W. Fonda, J.F. Bingert, K.J. Colligan, Development of grain structure during friction stir welding, Scr. Mater. 51 (2004) 243–248.
[20] J. Jeon, S. Mironov, Y. Sato, H. Kokawa, S. Park, S. Hirano, Grain structure development during friction stir welding of single-crystal austenitic stainless steel, Metall. Mater. Trans. A 44 (2013) 3157–3166.
[21] P.B. Prangnell, C.P. Heason, Grain structure formation during friction stir welding observed by the 'stop action technique', Acta Mater. 53 (2005) 3179–3192.
[22] T. Saeid, A. Abdollah-zadeh, T. Shibayanagi, K. Ikeuchi, H. Assadi, On the formation of grain structure during friction stir welding of duplex stainless steel, Mater. Sci. Eng. A 527 (2010) 6484–6488.
[23] J.-Q. Su, T.W. Nelson, C.J. Sterling, Microstructure evolution during FSW/FSP of high strength aluminum alloys, Mater. Sci. Eng. A 405 (2005) 277–286.
[24] T.R. McNelley, S. Swaminathan, J.Q. Su, Recrystallization mechanisms during friction stir welding/processing of aluminum alloys, Scr. Mater. 58 (2008) 349–354.
[25] U.F.H.R. Suhuddin, S. Mironov, Y.S. Sato, H. Kokawa, C.W. Lee, Grain structure evolution during friction-stir welding of AZ31 magnesium alloy, Acta Mater. 57 (2009) 5406–5418.
[26] S. Mironov, K. Inagaki, Y.S. Sato, H. Kokawa, Microstructural evolution of pure copper during friction-stir welding, Philos. Mag. 95 (2015) 367–381.
[27] F.J. Humphreys, M. Hatherly, Chapter 13 — hot deformation and dynamic restoration, in: F.J.H. Hatherly (Ed.), Recrystallization and Related Annealing Phenomena, second ed.Elsevier, Oxford 2004, p. 415-V.
[28] A. Heidarzadeh, K. Kazemi-Choobi, H. Hanifian, Asadi P. 3 — microstructural evolution, in: M.K.B. Givi, P. Asadi (Eds.), Advances in Friction-Stir Welding and Processing, Woodhead Publishing 2014, pp. 65–140.
[29] T. Sakai, A. Belyakov, R. Kaibyshev, H. Miura, J.J. Jonas, Dynamic and post-dynamic recrystallization under hot, cold and severe plastic deformation conditions, Prog. Mater. Sci. 60 (2014) 130–207.
[30] R.W. Fonda, K.E. Knipling, D.J. Rowenhorst, EBSD analysis of friction stir weld textures, JOM 66 (2014) 149–155.
[31] M.J. Starink, S.C. Wang, A model for the yield strength of overaged Al–Zn–Mg–Cu alloys, Acta Mater. 51 (2003) 5131–5150.
[32] M.J. Starink, A. Deschamps, S.C. Wang, The strength of friction stir welded and friction stir processed aluminium alloys, Scr. Mater. 58 (2008) 377–382.
[33] S. Wang, Z. Zhu, M. Starink, Estimation of dislocation densities in cold rolled Al–Mg–Cu–Mn alloys by combination of yield strength data, EBSD and strength models, J. Microsc. 217 (2005) 174–178.